IEEE Open Journal of
Industry Applications

Received 4 March 2024; revised 16 June 2024 and 30 July 2024; accepted 3 August 2024. Date of publication 12 August 2024; date of current version 20 August 2024. The review of this article was arranged by Associate Editor M. Di Nardo.

Digital Object Identifier 10.1109/OJIA.2024.3441308

Optimization of Analytical TSFs for DC-Link Current Reduction in Switched Reluctance Motors

FILIPE PINARELLO SCALCON [1] (Member, IEEE), GAOLIANG FANG [2] (Member, IEEE), CESAR JOSÉ VOLPATO FILHO [3] (Member, IEEE), SUMEDH DHALE [4] (Member, IEEE), AND BABAK NAHID-MOBARAKEH [5] (Fellow, IEEE)

[1]Department of Electrical and Software Engineering, University of Calgary, Calgary, AB T2N 1N4, Canada
[2]Faculty of Sustainable Design Engineering, University of Prince Edward Island, Charlottetown, PEI C1A 4P3, Canada
[3]Siemens Gamesa Renewable Energy A/S, 7330 Brande, Denmark
[4]Enedym Inc., Hamilton, ON L8P 0A1, Canada
[5]McMaster Automotive Resource Centre, McMaster University, Hamilton, ON L8P 0A6, Canada

CORRESPONDING AUTHOR: FILIPE PINARELLO SCALCON (e-mail: filipe.scalcon@ucalgary.ca)

This work was supported in part by Mitacs and industrial partner Enedym.

ABSTRACT The large dc-link current is a known issue in switched reluctance motor (SRM) drives, which often demand the use of a bulky dc-link capacitor. However, control techniques can be designed and optimized to lessen this issue. In this context, this article proposes the optimization of analytical torque sharing functions (TSFs) for dc-link current reduction in SRMs. Initially, the analytical TSFs are described, and the importance of adequate parameter selection is highlighted. Next, an optimization procedure based on the nondominated sorting genetic algorithm II is proposed to determine the optimal turn-ON and overlap angles by solving a multiobjective optimization problem considering torque rms error and dc-link rms current as objectives to be minimized, something not previously reported in the literature. The pareto fronts for different operating conditions are presented, including both soft and hard chopping operation, as well as different sampling frequencies. Then, an approach for selecting a solution from within the pareto front is described, enabling the result from the pareto front that yielded the desired tradeoff between torque RMSE and dc-link current to be identified. Experimental results are provided to support the effectiveness of the proposal. A comparison between three different cases is shown, highlighting the tradeoff between objectives.

INDEX TERMS Dc-link current, optimization, switched reluctance motor (SRM), torque sharing function (TSF).

I. INTRODUCTION

In the search for rare-Earth-free machines, the switched reluctance motor (SRM) has emerged as a prime candidate. The SRM has several advantages, such as robustness, low manufacturing costs, inherent fault-tolerance, and a simple structure. In addition, the rotor of the machine is free of any permanent magnets, which present price fluctuations, supply chain restrictions, and significant environmental impact. These features make the machine an ideal candidate for propulsion applications, for example [1], [2], [3], [4], and [5]. High torque ripple and acoustic noise are known challenges of the machine, which have been studied and addressed mainly through adequate machine design and high-performance control strategies [6], [7], [8], [9], [10].

Another challenge of SRMs is the need for a large dc-link capacitor, which results in an increase in the cost and volume of the system. Due to the switched nature of the machine, a large amount of energy is exchanged between the dc-link and the phases during magnetization and demagnetization, leading to significant voltage and current ripple [11]. In addition, large rms capacitor current is often observed in SRMs, which leads to an increase in capacitor temperature and, in turn, a reduction in the lifetime of the component [12]. Thus, a bulky capacitor is often required to suppress these fluctuations and

to help provide the drive with the necessary energy, while also ensuring a suitable operating temperature. One effective technique for reducing the capacitor size in SRM drives is through the minimization of rms capacitor and dc-link currents [13].

In this context, the reduction of dc-link and capacitor rms currents has become a topic of interest [14], [15], [16], [17], [18], [19], [20]. A method for dc-link and capacitor rms current evaluation in SRM drives is proposed in Ahmad and Narayanan's [14] work. In Klein-Hessling et al.'s [15] work, an additional dc–dc converter is used in order to reduce the dc-link capacitor. Similar hardware-based approaches to promoting capacitor reduction in SRM drives are also observed in [16] and [17], for example. Although successful, these proposals increase the complexity and cost of the system. A synchronized switching modulation strategy to reduce dc-link current is proposed in Cabezuelo et al.'s [18] work. By forcing the exchange of energy between phases, authors are able to decrease the energy transfer between the dc-link and the machine. Similarly, in Neuhaus et al.'s [19] work, a control scheme with power balancing phase commutation is proposed. The magnetic energy is kept within the machine and used to magnetize the incoming phase, allowing the dc-link capacitance to be minimized. In Haque et al.'s [20] work, a closed-loop dc-link current ripple minimization algorithm is developed. Based on the input dc-link current measurement, the phase currents are shaped in order to reduce current ripple and deliver smooth torque. Note, however, that few dc-link current reduction strategies with torque ripple reduction capabilities have been investigated.

Torque sharing functions (TSFs) are an effective approach at torque ripple reduction, and can often be optimized in order to account for a secondary objective [21], [22], [23], [24], [25]. In Xue et al.'s [21] work, a genetic algorithm is used to optimize the turn-ON and overlap angles of TSFs to minimize copper losses while extending the speed range. An analytical approach is presented in Vujičić's [22] work, also delivering torque-ripple minimization with optimal efficiency. An optimized TSF is described in Ye et al.'s [23] work, where the square of phase currents and the rate of change of flux linkage are both considered as secondary metrics for optimization. Finally, more recent approaches, such as [24] and [25], have proposed offline optimized TSFs with reduced phase current while also featuring reduced computational burden and improved current tracking performance, respectively.

Although the above-mentioned presented strategies are able to effectively reduce phase currents, it should be noted, however, that this does not guarantee that the dc-link current is effectively being reduced. In addition, to the best of our knowledge, no attempt of TSF optimization considering dc-link related metrics has been observed in literature to date. In this context, this article presents as a contribution an original analysis of the capabilities of dc-link current reduction by means of optimization applied to analytical TSFs. First, the analytical TSFs are presented, and the effects of adequate parameter selection are illustrated. Then, unlike what has been previously reported in the literature, a multiobjective optimization procedure is used to optimize the TSFs with respect to torque rms error (RMSE) and dc-link rms current, making use of the nondominated sorting genetic algorithm II (NSGA-II). The pareto fronts along with the optimal firing angles are presented to demonstrate the effectiveness of the optimization approach for both hard chopping (HC) and soft chopping (SC) operation. The cost functions are combined by using normalization, enabling an optimal result with the desired tradeoff to be identified. Experimental results are presented to demonstrate the effectiveness of the proposal, comparing different optimal solutions with the selected optimal result from the pareto front, as well as highlighting the tradeoff between optimization and performance metrics.

II. SRM FUNDAMENTALS

This section presents the mathematical modeling of the SRM, the asymmetric half-bridge converter, and the control fundamentals regarding HC, SC, and dc-link current.

A. SRM MODEL

The SRM presents excitation exclusively on its stator, given the absence of magnets or windings in its rotor [1]. By neglecting phase coupling, the SRM phase voltage is given by

$$v_{\text{ph}} = Ri + \frac{d\lambda}{dt} \tag{1}$$

where v_{ph} is the phase voltage, R is the winding resistance, i is the phase current, and λ is the flux linkage. As a result of the double salient structure of the machine, flux linkage is a nonlinear function of both current and rotor position, θ

$$\lambda(i, \theta) = L(i, \theta)i(t). \tag{2}$$

Substituting (2) in (1) and rewriting the terms results

$$v_{\text{ph}} = Ri + l(\theta, i)\frac{di}{dt} + e \tag{3}$$

where

$$l(\theta, i) = L(\theta, i) + i\frac{\partial L(\theta, i)}{\partial i} \tag{4}$$

$$e = i\omega_r \frac{\partial L(\theta, i)}{\partial \theta}. \tag{5}$$

The first term, $l(\theta, i)$, is referred to as incremental inductance [26]. It accounts for the effects of magnetic saturation, by considering current, self-inductance $L(\theta, i)$ and the inductance variation caused by current. The term e corresponds to the machine's back-EMF, where ω_r is the rotor speed.

B. ASYMMETRIC HALF-BRIDGE CONVERTER

Due to the switched nature of the machine, the use of a static converter is required for SRMs. The most commonly used topology is the asymmetric half-bridge converter [27], where a four-phase configuration is depicted in Fig. 1.

Assuming that each phase is excited independently, without overlapping, the switching states of the converter can be analyzed separately, as depicted in Fig. 2. First, when both

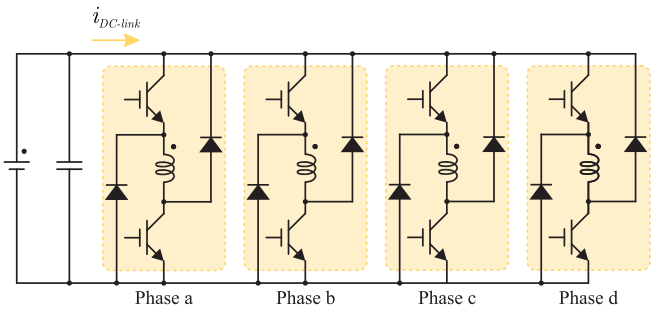

FIGURE 1. Four-phase asymmetric half-bridge converter.

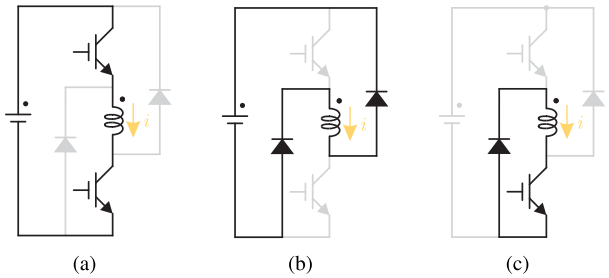

FIGURE 2. Switching states for the asymmetric half-bridge converter. (a) Magnetization. (b) Demagnetization. (c) Freewheeling.

of the switched are closed, dc-link voltage is applied to the phase and current rises, characterizing the state of magnetization, as shown in Fig. 2(a). Note that during this state the diodes are blocked. Once the switches are opened, negative dc-link voltage is applied to the phase, causing the diodes to be forward biased and current to decrease characterizing the demagnetization state, shown in Fig. 2(b). During this state, current returns to the dc-link until phase current reaches zero, when the diodes no longer conduct. Finally, a third switching state can be used, where one of the switches is closed and the other is open. This causes the phase current to flow within the phase, a switch and a diode, characterizing the freewheeling state, shown in Fig. 2(c). Note that this state is of interest, as it does not contribute to the dc-link current.

C. SRM CONTROL AND DC-LINK CURRENT

The control of an SRM is dependent on the rotor speed. By disregarding the phase resistance, (3) can be rewritten as

$$v_{\text{ph}} - e = l(\theta, i)\frac{di}{dt}. \tag{6}$$

From (6), it can be observed that as long as the excitation voltage has a greater magnitude than the back-EMF, phase current can be controlled. The point at which current control is no longer feasible in SRMs is also often referred to as base speed [3].

When operating in the current controlled region, a hysteresis controller is often used in order to regulate current during the excitation period. Considering the switching states of the asymmetric half-bridge converter presented in Fig. 2,

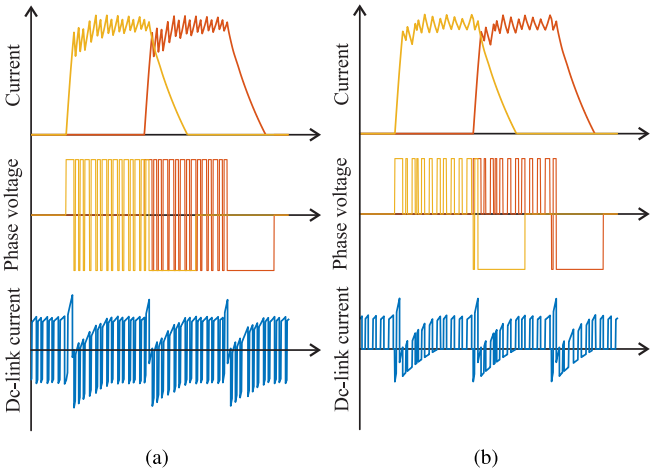

FIGURE 3. Example waveforms for phase current, phase voltage, and dc-link current. (a) HC. (b) SC.

the most common topology used to drive an SRM, two different excitation approaches can be employed: HC and SC. In HC only positive and negative voltage levels [see Fig. 2(a) and (b)] are applied, while in SC positive and zero voltage levels [see Fig. 2(a) and (c)] are used during excitation and negative voltage [see Fig. 2(b)] is only used to demagnetize the winding toward the end of the excitation period.

In order to demonstrate the effects of both HC and SC in the dc-link current, example waveforms are presented in Fig. 3. It can be seen that the use of HC contributes to dc-link current during both magnetization and demagnetization. When using SC, however, due to the freewheeling state, current does not return to the dc-link, effectively reducing rms dc-link current.

III. TORQUE SHARING FUNCTIONS

TSFs are an effective tool for torque ripple reduction in SRM drives. The technique shares the torque production between the active phases, ensuring that the total torque produced equals the desired reference value. During commutation, torque is shared by gradually increasing torque production of the incoming phase and reducing torque production of the outgoing phase [6].

A. ANALYTICAL TSFS

Considering phase h of an SRM, the torque reference is defined as

$$T_{\text{ref}-h} = \begin{cases} 0 & 0 \le \theta < \theta_{\text{on}} \\ T_{\text{ref}} \times f_{\text{rise}}(\theta) & \theta_{\text{on}} \le \theta < \theta_{\text{on}} + \theta_{\text{ov}} \\ T_{\text{ref}} & \theta_{\text{on}} + \theta_{\text{ov}} \le \theta < \theta_{\text{off}} \\ T_{\text{ref}} \times f_{\text{fall}}(\theta) & \theta_{\text{off}} \le \theta < \theta_{\text{off}} + \theta_{\text{ov}} \\ 0 & \theta_{\text{off}} + \theta_{\text{ov}} \le \theta < \theta_{\text{off}} + \theta_p \end{cases} \tag{7}$$

where $T_{\text{ref}-h}$ is the torque reference for phase h, T_{ref} is the total torque reference, $f_{\text{rise}}(\theta)$ is the rising portion of the TSF, $f_{\text{fall}}(\theta)$ is the falling portion of the TSF, θ_{on} is the turn-ON

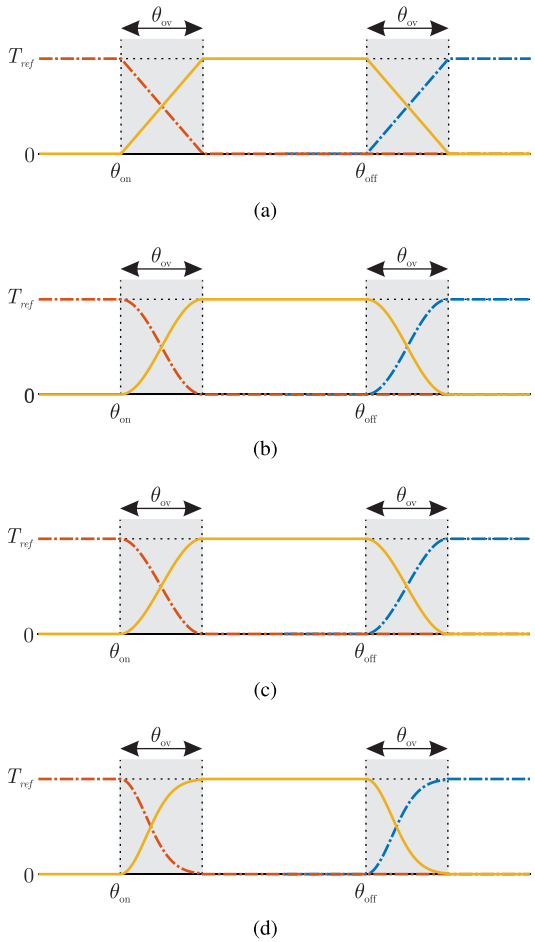

FIGURE 4. Analytical TSFs. (a) Linear. (b) Sinusoidal. (c) Cubic. (d) Exponential.

angle, θ_{off} is the turn-OFFangle, θ_{ov} is the overlap angle, θ_p is the pole pitch, and θ is the phase position.

Analytical TSFs, also referred to as conventional TSFs, make use of mathematical expressions to share the torque in the overlap region [6]. Fig. 4 depicts the linear, sinusoidal, exponential and cubic TSFs, the most commonly used in literature.

According to Xue et al. [21], the different rising and falling portions of the four TSFs shown in Fig. 4 can be computed according to the following.

1) Linear TSF

$$f_{\text{rise}}^{\text{lin}}(\theta) = \frac{1}{\theta_{\text{ov}}}(\theta - \theta_{\text{on}}) \tag{8}$$

$$f_{\text{fall}}^{\text{lin}}(\theta) = 1 - \frac{1}{\theta_{\text{ov}}}(\theta - \theta_{\text{off}}). \tag{9}$$

2) Sinusoidal TSF

$$f_{\text{rise}}^{\text{sin}}(\theta) = \frac{1}{2} - \frac{1}{2}\cos\frac{\pi}{\theta_{\text{ov}}}(\theta - \theta_{\text{on}}) \tag{10}$$

$$f_{\text{fall}}^{\text{sin}}(\theta) = \frac{1}{2} + \frac{1}{2}\cos\frac{\pi}{\theta_{\text{ov}}}(\theta - \theta_{\text{off}}). \tag{11}$$

TABLE 1. Current Metrics for the Different Current Profiles

	θ_{on}	θ_{ov}	θ_{off}	Peak current	Rms current
Profile A1	3°	5°	18°	23.79 A	8.54 A
Profile A2	4°	5°	19°	18.28 A	7.80 A
Profile A3	5°	5°	20°	14.54 A	7.40 A
Profile A4	6°	5°	21°	14.57 A	7.25 A
Profile B1	5°	3°	20°	19.21 A	7.67 A
Profile B2	5°	4°	20°	15.70 A	7.50 A
Profile B3	5°	5°	20°	14.54 A	7.40 A
Profile B4	5°	6°	20°	14.54 A	7.34 A

3) Exponential TSF

$$f_{\text{rise}}^{\text{exp}}(\theta) = 1 - \exp\left(\frac{-(\theta - \theta_{\text{on}})^2}{\theta_{\text{ov}}}\right) \tag{12}$$

$$f_{\text{fall}}^{\text{exp}}(\theta) = \exp\left(\frac{-(\theta - \theta_{\text{off}})^2}{\theta_{\text{ov}}}\right). \tag{13}$$

4) Cubic TSF

$$f_{\text{rise}}^{\text{cub}}(\theta) = \frac{3}{\theta_{\text{ov}}^2}(\theta - \theta_{\text{on}})^2 - \frac{2}{\theta_{\text{ov}}^3}(\theta - \theta_{\text{on}})^3 \tag{14}$$

$$f_{\text{fall}}^{\text{cub}}(\theta) = 1 - \frac{3}{\theta_{\text{ov}}^2}(\theta - \theta_{\text{off}})^2 + \frac{2}{\theta_{\text{ov}}^3}(\theta - \theta_{\text{off}})^3. \tag{15}$$

Note that for the TSFs presented previously, the overlap angle must meet [21]

$$\theta_{\text{ov}} \leq \frac{\theta_p}{2} - \theta_{\text{off}}. \tag{16}$$

From Fig. 4, the turn-OFF angle is given by

$$\theta_{\text{off}} = \theta_{\text{on}} + \theta_{\text{shift}} \tag{17}$$

where θ_{shift} is the mechanical phase shift between adjacent phases. In the case of the machine used in this article, a four-phase 8/6 SRM, a pole pitch of 60° and a shift of 15° are observed. Hence, (16) can be rewritten as

$$\theta_{\text{ov}} \leq 15 - \theta_{\text{on}}. \tag{18}$$

B. PARAMETER SELECTION

Once the phase torque references are obtained, an inverted torque lookup table (LUT), $i(\theta, T)$ LUT, is used in order to acquire the phase current references. Although different turn-ON and overlap angle combinations will generate similar torque references for a given TSF, due to the highly nonlinear torque–current–position characteristic of SRMs, the reference currents will vary significantly. In order to illustrate this phenomenon, Fig. 5 shows eight different current references for a linear TSF using the angle combinations presented in Table 1. Peak and rms current measurements for every profile are also provided.

It can be seen that the current profiles are directly affected by the changes in the turn-ON and overlap angles. In addition, it is observed that the peak and rms current values are also impacted by the excitation interval. Note, however,

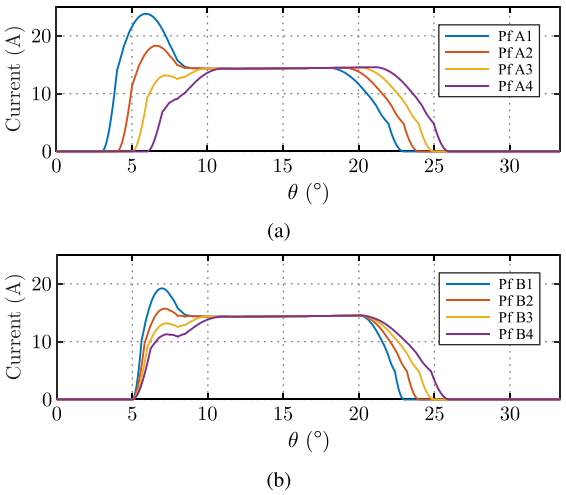

FIGURE 5. Phase current profiles generated by TSFs with different angle combinations. (a) Different θ_{on} values. (b) Different θ_{ov} values.

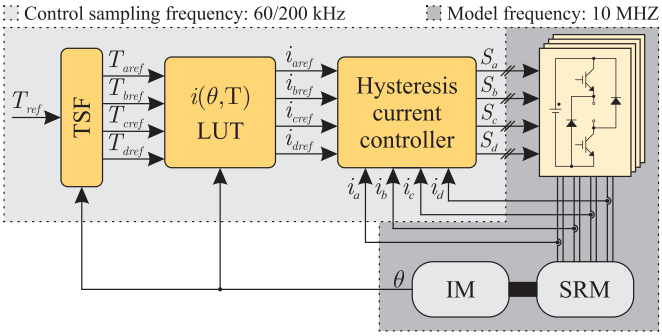

FIGURE 6. Block diagram of the SRM control structure.

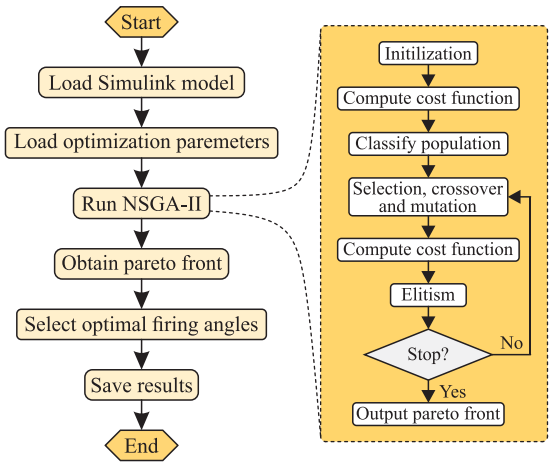

FIGURE 7. Flowchart of the proposed TSF optimization procedure.

that different profiles may present different advantages when compared to one another. Hence, the adequate choice of the TSF parameters is key for optimal performance.

In the following subsection, a multiobjective optimization algorithm for analytical TSFs will be proposed.

IV. TSF OPTIMIZATION PROCEDURE

The optimization procedure proposed in this section aims to determine the optimal turn-ON and overlap angles for analytical TSFs seeking to reduce dc-link current and torque RMSE. A case study for an 8/6 SRM illustrates the use of the procedure.

A. OPTIMIZATION PROCEDURE

The algorithm chosen for this proposal is NSGA-II [28]. Two cost functions are defined to guide such algorithm, where the objective of the optimization procedure is to minimize both of the cost functions as much as possible, yielding a pareto front of optimal solutions. The first function, $f_1(\theta_{on}, \theta_{ov})$, is a measure of the torque RMSE, T_{RMSE}, while the second function, $f_2(\theta_{on}, \theta_{ov})$, is a measure of the rms value of the dc-link current, $i_{dc\text{-}link}$. Both functions are shown in (19) and (20), respectively

$$f_1(\theta_{on}, \theta_{ov}) = \sqrt{\frac{1}{N}\sum_{k=1}^{N}\left(T_{ref(k)} - T_{e(k)}\right)^2} \tag{19}$$

$$f_2(\theta_{on}, \theta_{ov}) = \sqrt{\frac{1}{N}\sum_{k=1}^{N}\left(i_{dc\text{-}link(k)}\right)^2} \tag{20}$$

where T_e is the total electromagnetic torque and N is the number of data points. Moreover, note that the optimization algorithm is subject to the linear constraint given in (16).

A simulation model is built in MATLAB/Simulink software. The control structure used is depicted in Fig. 6. A torque reference is used along with a TSF to generate the individual phase torque references. Then, the inverted torque LUT, $i(\theta, T)$ LUT, is used in order to obtain the phase current references. Finally, a hysteresis controller is used to track the current references. Based on the output of the hysteresis controller, adequate switching signals are generated and sent to the asymmetric half-bridge converter.

The proposed optimization procedure is shown in Fig. 7. It is performed entirely offline, and it starts by loading the SRM simulation model in Simulink. Next, the optimization parameters are loaded, such as the parameter bounds, inequality constraints and the population size. Then, the execution of the NSGA-II starts. At the end of each simulation, the cost functions are calculated, and the population of the GA is updated. The steps of the NSGA-II algorithm are depicted in Fig. 7, and for a detailed explanation, please refer to Deb et al.'s [28] work. The algorithm is executed until the stopping criterion is met, which in this case is determined by the average change in the spread of the pareto solutions over a number of maximum stall generations. From the pareto front, a solution that suits the desired balance between cost functions can be selected.

TABLE 2. Parameters of the Studied SRM

Parameter	Value
Rated speed	6000 r/min
Rated power	5.1 kW
Rated voltage	300 V
Number of phases	4
Stator poles	8
Rotor poles	6

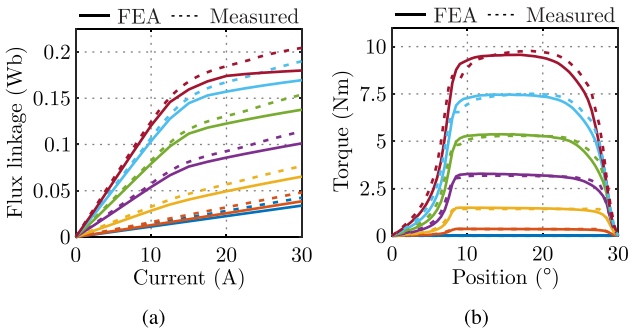

FIGURE 8. Characteristics of the 8/6 SRM. (a) Flux linkage. (b) Torque.

First, the vectors containing the cost function values for the optimal results from the pareto front can be defined as

$$F_1 = \begin{bmatrix} f1_{(1)} & f1_{(2)} & \cdots & f1_{(n)} \end{bmatrix}^T \tag{21}$$

$$F_2 = \begin{bmatrix} f2_{(1)} & f2_{(2)} & \cdots & f2_{(n)} \end{bmatrix}^T \tag{22}$$

where n is the number of solutions in the pareto front.

Then, F_1 and F_2 can be combined into a single metric by means of normalization, where both of the cost functions are normalized with respect to their maximum observed value, as shown in the following:

$$F_{\text{norm}} = \alpha \frac{F_1}{\max\left[F_1\right]} + \beta \frac{F_2}{\max\left[F_2\right]} \tag{23}$$

where F_{norm} is the normalized cost function vector, and α and β are weights.

The firing angles that yielded the minimal value of F_{norm} are saved, and the procedure is repeated for different operating conditions.

B. CASE STUDY

This subsection presents a case study for the optimized analytical TSFs with reduced dc-link current.

The characteristics of the SRM used in this article are given in Table 2. The flux linkage and torque profiles of the machine are presented in Fig. 8. The first set of characteristics is obtained by means of finite element analysis data, using JMAG software. The second set, labeled measured, is obtained using the dc excitation method [29], with the rotor locked mechanically.

The optimization parameters used are given in Table 3. The linear constraint is set based on the condition presented in (18), ensuring that $\theta_{\text{on}} + \theta_{\text{ov}} \leq 15$. Furthermore, the initial population of the NSGA-II is initialized randomly. The stopping criteria of the optimization procedure is determined by the average relative change in the best fitness function value over a maximum number of stall generations. If this value is less than or equal to the "function tolerance" parameter over a number of "maximum stall generations," the algorithm will be stopped.

TABLE 3. Parameters of the NSGA II Implementation

Parameter	Value
Population size	30
θ_{on} bounds	[0°,15°]
θ_{ov} bounds	[0°,15°]
Function tolerance	10^{-4}
Maximum stall generations	100

Simulation results are obtained using MATLAB/Simulink software. The sampling frequency of the control algorithm is set to 200 kHz to ensure the hysteresis controller has superior current tracking performance. In addition, results considering a 60 kHz sampling frequency are also presented as a means to investigate the effects of the sampling rate in the torque RMSE and dc-link current. Regardless of the control frequency, the simulation frequency for the model is set to 10 MHz, as depicted in Fig. 6. For real-world applications, an advanced PWM current controller could be used as an alternative. The hysteresis band is set to 0.5 A and both HC and SC operations are investigated. For HC, only the positive and negative voltage levels are used, while SC uses the positive, zero and negative voltage levels. Note that, in this article, SC operation is implemented as proposed in Scalcon et al.'s [30] work, where positive and zero voltage levels are applied while $\theta < \theta_{\text{off}}$, while positive and negative voltage levels are applied after $\theta > \theta_{\text{off}}$.

The algorithm is executed for the four different TSFs presented in Fig. 4. The optimization results for a speed of 1000 r/min at a 3 Nm load, composed of the pareto sets and the optimal firing angles, are presented in Fig. 9. The results consider both HC and SC, as well as 200 and 60 kHz sampling frequencies. Similarly, Figs. 10 and 11 present results for the operating conditions of 3000 r/min at 3 Nm and 6000 r/min at 1.5 Nm, respectively.

First, a tradeoff between both cost functions is observed. Moreover, it can be seen that the dc-link current can be reduced to a certain extent while exhibiting reasonable torque tracking error. Furthermore, a similar behavior can be observed for the results using HC, despite of the different operating conditions. When considering SC, however, a bigger discrepancy between the different TSFs is observed. This is made evident in Fig. 10(b) and (d), as well as in Fig. 11(b) and (d). It should be noted, however, that the exponential TSF tends to perform worse when compared to the remaining three TSFs. When comparing both HC and SC, it can be observed that SC is able to significantly reduce dc-link current. This

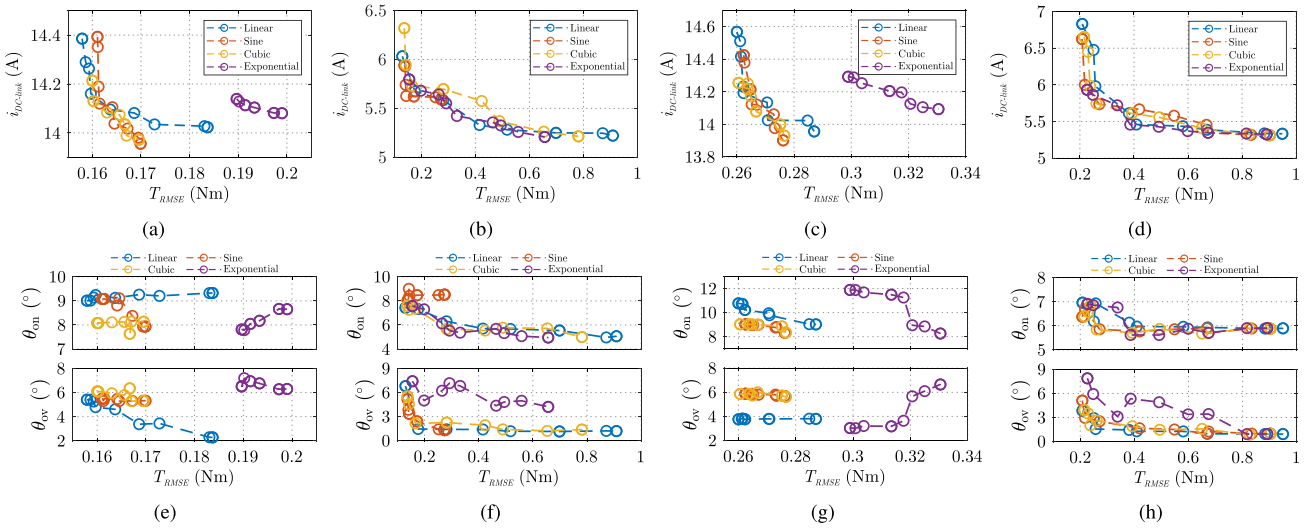

FIGURE 9. Optimization results for a speed of 1000 r/min at a 3 Nm load. (a) Pareto fronts for 200 kHz and HC. (b) Pareto fronts for 200 kHz and SC. (c) Pareto fronts for 60 kHz and HC. (d) Pareto fronts for 60 kHz and SC. (e) Optimal angles for 200 kHz and HC. (f) Optimal angles for 200 kHz and SC. (g) Optimal angles for 60 kHz and HC. (h) Optimal angles for 60 kHz and SC.

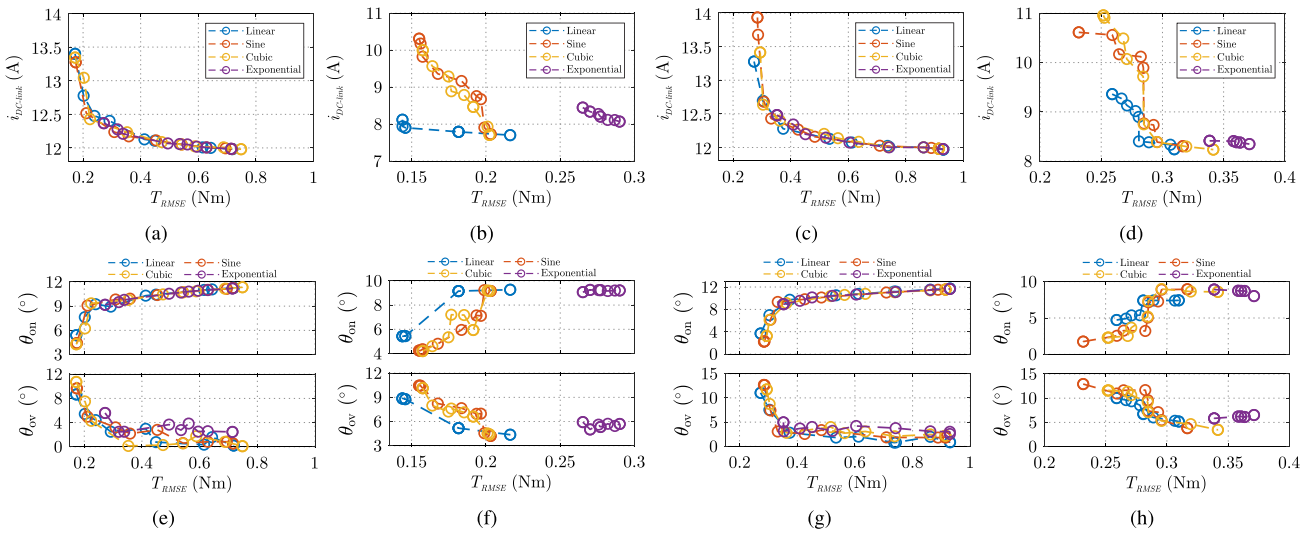

FIGURE 10. Optimization results for a speed of 3000 r/min at a 3 Nm load. (a) Pareto fronts for 200 kHz and HC. (b) Pareto fronts for 200 kHz and SC. (c) Pareto fronts for 60 kHz and HC. (d) Pareto fronts for 60 kHz and SC. (e) Optimal angles for 200 kHz and HC. (f) Optimal angles for 200 kHz and SC. (g) Optimal angles for 60 kHz and HC. (h) Optimal angles for 60 kHz and SC.

is attributed to the fact that the hysteresis current controller switches between positive and zero voltage levels for most of the excitation period, which causes no contribution to the dc-link current during the freewheeling state. On the other hand, HC uses both positive and negative voltage levels, constantly contributing to dc-link current. Regarding the torque tracking performance, it can be observed that at lower speeds, HC enables superior tracking, while SC exhibits different tracking capability along the pareto front. With the increase in speed, however, HC also presents a larger tradeoff on its pareto fronts. It should be noted that, even though reasonable results are also observed at higher speed conditions, TSFs progressively lose current tracking capabilities with the increase of speed, and, consequently, torque tracking capability. Hence, this technique is not suitable for high-speed conditions, with typically single pulse control being used above base speed.

Regarding sampling frequency, it can be seen that a lower sampling rate leads to worse torque tracking performance. This is demonstrated by the higher torque RMSE values observed in the results with 60 kHz when compared to the 200 kHz counterpart. This is expected, as the current tracking performance of the hysteresis controller is directly related to

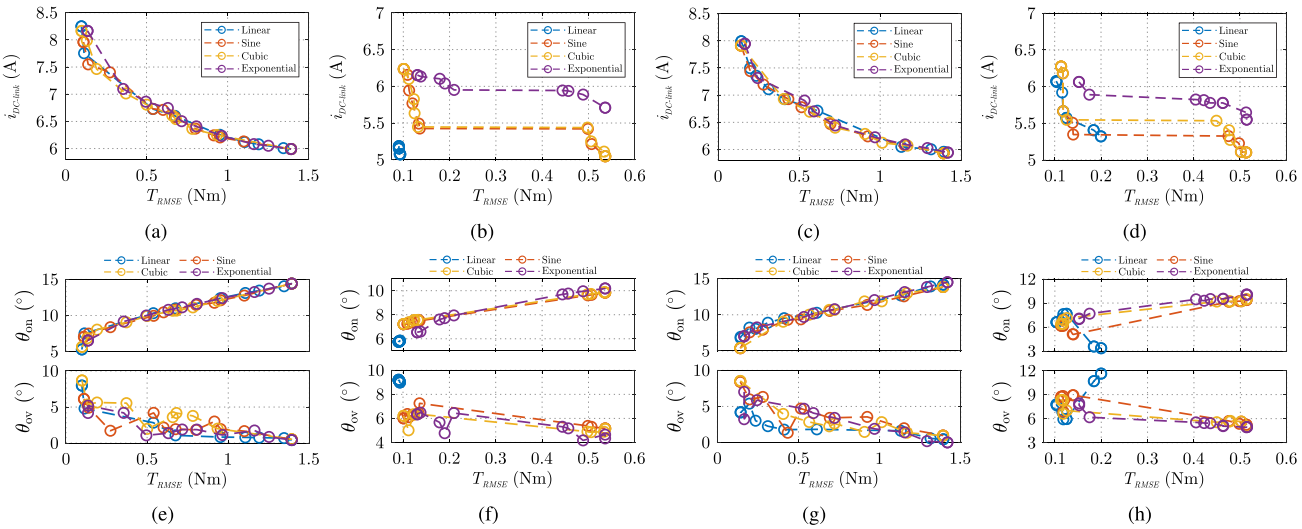

FIGURE 11. Optimization results for a speed of 6000 r/min at a 1.5 Nm load. (a) Pareto fronts for 200 kHz and HC. (b) Pareto fronts for 200 kHz and SC. (c) Pareto fronts for 60 kHz and HC. (d) Pareto fronts for 60 kHz and SC. (e) Optimal angles for 200 kHz and HC. (f) Optimal angles for 200 kHz and SC. (g) Optimal angles for 60 kHz and HC. (h) Optimal angles for 60 kHz and SC.

the sampling rate. For the high-speed results, at 6000 r/min, it is observed that the gap in performance between the different frequencies is much smaller. This can be attributed to the fact that, with the increase in speed, the back-EMF of the machine is also increased, generally deteriorating the tracking capability of the controller at higher speeds. Furthermore, the ratio between sampling and electrical frequencies is much closer than it is at lower speeds, justifying the similar performance.

Finally, it can be seen that solutions that yielded lower torque RMSE typically present a larger overlap angle, while solutions that more effectively minimize the dc-link current tend to have a smaller overlap angle. In addition, with the increase in speed, the turn-ON angle is advanced in solutions with good torque tracking performance. This is an expected behavior in SRMs, that can be seen replicated here in the results of the optimization procedure.

Based on these solutions, a point from the pareto front which satisfies the desired dc-link current reduction, while still presenting an acceptable torque RMSE value, can be selected as the optimal firing angles by means of (23). For this article, authors opted to use $\alpha = 1$ and $\beta = 2$, due to the normalized variation in torque RMSE being much greater than the variation in dc-link current. Please note, however, that the weights should be adjusted according to the studied SRM, application and targeted dc-link current reduction.

Experimental results will be presented in the following section as a means to compare the performance of different solutions from the pareto front.

V. EXPERIMENTAL RESULTS

In order to verify the effectiveness of the proposed optimization procedure, experimental results are presented in this section. The machine used is the 8/6 SRM described in Section IV-B. The experimental setup is presented in Fig. 12,

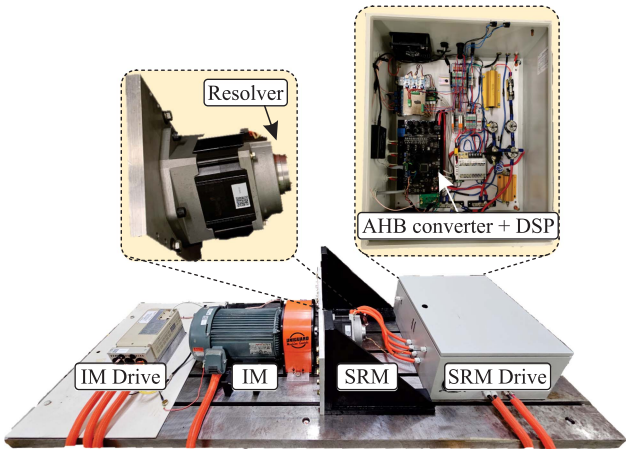

FIGURE 12. Experimental setup containing the SRM, IM, and their respective drives.

being mainly composed of an SRM coupled to an induction machine (IM), a four-phase AHB converter and a commercial three-phase IM drive. The IM is used as a means to provide a mechanical load to the SRM by operating as a generator. A TS2225N13E102 resolver, built-in to the SRM housing, is used to measure the rotor position.

Fig. 6 depicts the block diagram of the proposed control structure. A digital signal processor (DSP) TMS320F28335 is used for digital implementation. The hysteresis current controller uses a hysteresis band of 1 A with a 55 kHz sampling frequency, the highest achievable value considering the limited performance of this DSP [24]. Due to digital implementation, the hysteresis controller presents a one sample delay. Both HC and SC operation are evaluated experimentally. For SC, positive and zero voltage levels are applied

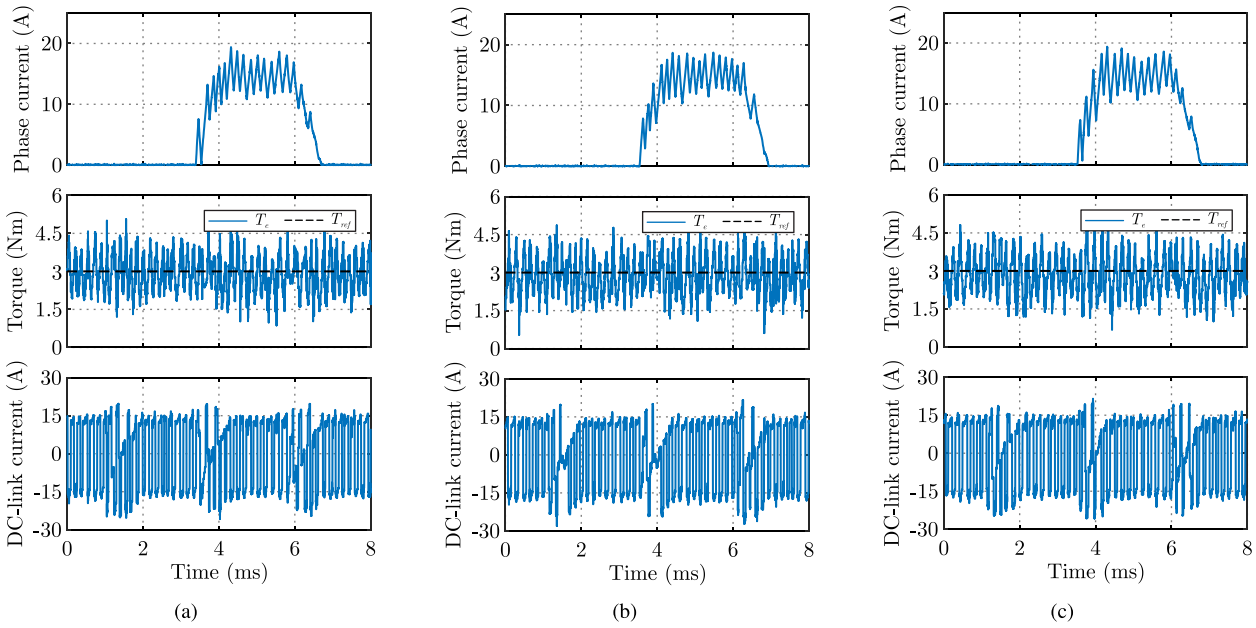

FIGURE 13. Experimental results for HC at a speed of 1000 r/min under a 3 Nm load. (a) Case 1. (b) Case 2. (c) Case 3.

while $\theta < \theta_{\text{off}}$, while positive and negative voltage levels are applied after $\theta > \theta_{\text{off}}$. For HC, only positive and negative voltage levels are used.

In addition, for each operation mode, three cases are considered as follows.

1) Case 1: result from the pareto front that yielded the smallest $f_1(\theta_{\text{on}}, \theta_{\text{ov}})$ (torque RMSE) value.
2) Case 2: result from the pareto front that yielded the desired tradeoff between torque RMSE and dc-link current according to (23).
3) Case 3: result from the pareto front that yielded the smallest $f_2(\theta_{\text{on}}, \theta_{\text{ov}})$ (dc-link current) value.

For the results presented in this article, the torque to current conversion is performed offline using Simulink, by means of an inverted torque LUT. Hence, the current references are loaded directly to the DSP's memory, and no online conversion is performed. The instantaneous torque waveforms, on the other hand, are estimated inside of the DSP by means of a torque LUT and measured using a 12-bit digital-to-analog converter. This LUT is obtained as described in Bilgin et al.'s [31] work, using characteristics of the studied SRM. It has as inputs the phase current and position measurements, while outputting the instantaneous phase torque value. The total torque is obtained by repeating the procedure for each phase and adding the individual results.

Fig. 13 shows the experimental results for the sinusoidal TSF for the three different cases considering HC operation at a speed of 1000 r/min under a 3 Nm load. Similarly, Fig. 14 shows experimental results for the sinusoidal TSF for the same cases and operating condition considering SC operation. In order to evaluate the proposal for a different operating speed, experimental results at 3000 r/min under a 3 Nm load considering hard and SC operation are presented in Figs. 15 and 16, respectively. The turn-ON and overlap angles used in the experimental results are extracted from Figs. 9 and 10, and given in Table 4.

TABLE 4. Excitation Parameters for the Experimental Results

Excitation	Case	1000 r/min		3000 r/min	
		θ_{on}	θ_{ov}	θ_{on}	θ_{ov}
HC	1	9.02°	5.88°	2.23°	12.67°
	2	8.99°	5.80°	6.14°	7.41°
	3	8.32°	5.69°	11.55°	1.81°
SC	1	6.38°	5.11°	1.75°	12.91°
	2	5.77°	1.66°	7.16°	7.34°
	3	5.88°	0.99°	8.96°	3.80°

From the results, it can be observed that SC is able to achieve significant dc-link current reduction when compared to HC. Moreover, a tradeoff between objectives is observed, with case 1 generally showing a lower torque RMSE value, while case 3 shows the most reduction in dc-link current. A quantitative analysis is shown in Tables 5 and 6, where measurements of T_{RMSE}, $i_{\text{dc-link}}$, torque ripple, efficiency and torque per ampere ratio are presented for the results shown in Figs. 13–16.

The torque ripple, T_{ripple}, is given by

$$T_{\text{ripple}} = \frac{T_{\text{max}} - T_{\text{min}}}{T_{\text{avg}}} \tag{24}$$

where T_{max} is the maximum estimated torque value, T_{min} is the minimum estimated torque value, and T_{avg} is the average torque value.

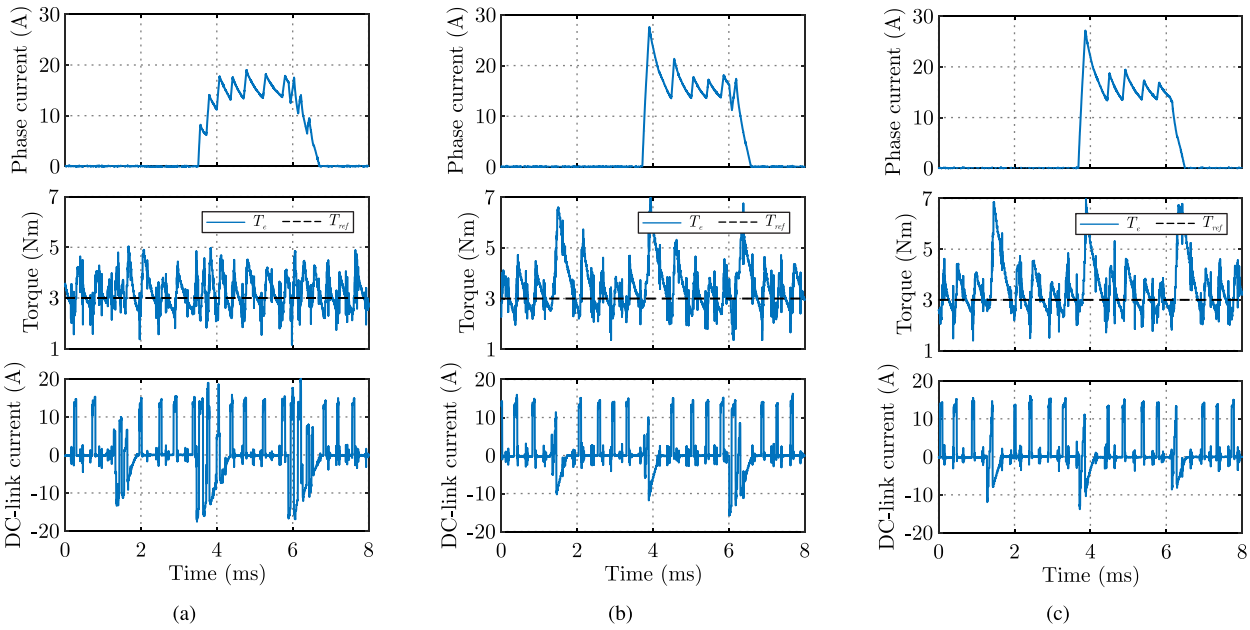

FIGURE 14. Experimental results for SC at a speed of 1000 r/min under a 3 Nm load. (a) Case 1. (b) Case 2. (c) Case 3.

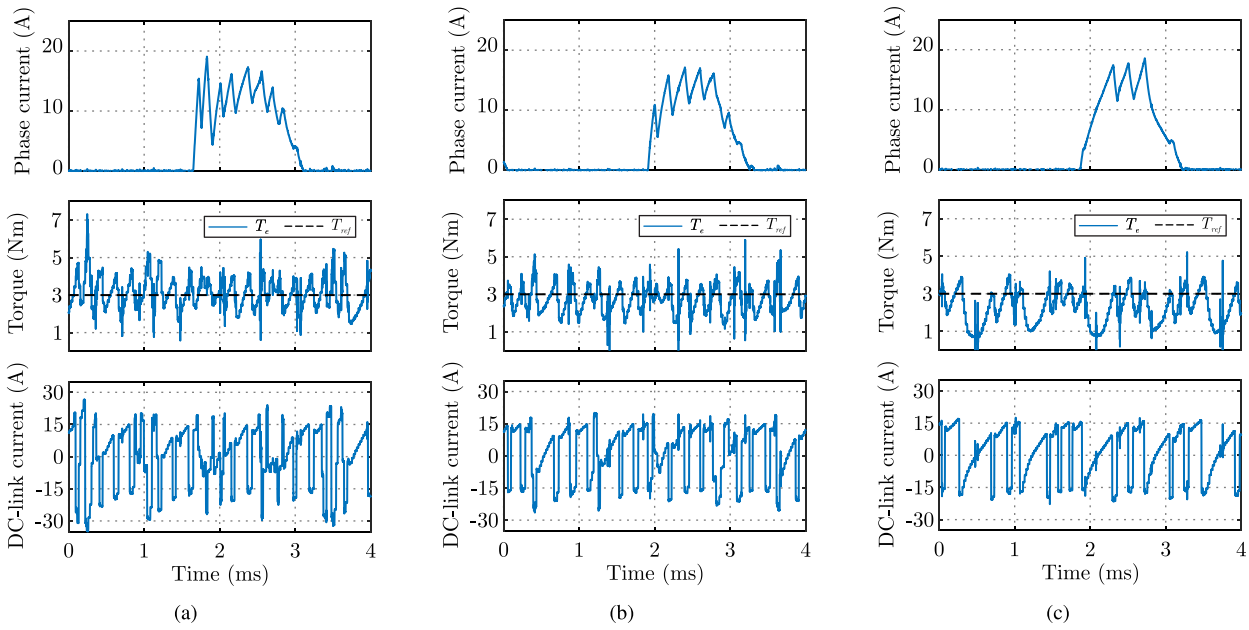

FIGURE 15. Experimental results for HC at a speed of 3000 r/min under a 3 Nm load. (a) Case 1. (b) Case 2. (c) Case 3.

The efficiency, η, is calculated as

$$\eta = \frac{P_{\text{out}}}{P_{\text{in}}} \tag{25}$$

where P_{in} is the input power and P_{out} is the output power.

The input power is defined as

$$P_{\text{in}} = V_{\text{dc}} i_{\text{avg}} \tag{26}$$

where V_{dc} is the dc-link voltage and i_{avg} is the average dc bus current.

The output power is defined as

$$P_{\text{out}} = \omega_r T_{\text{avg}}. \tag{27}$$

The torque per ampere ratio, another metric often used to evaluate efficiency [31], is calculated as $T_{\text{avg}}/i_{\text{rms}}$, where i_{rms} is the rms value of the phase current.

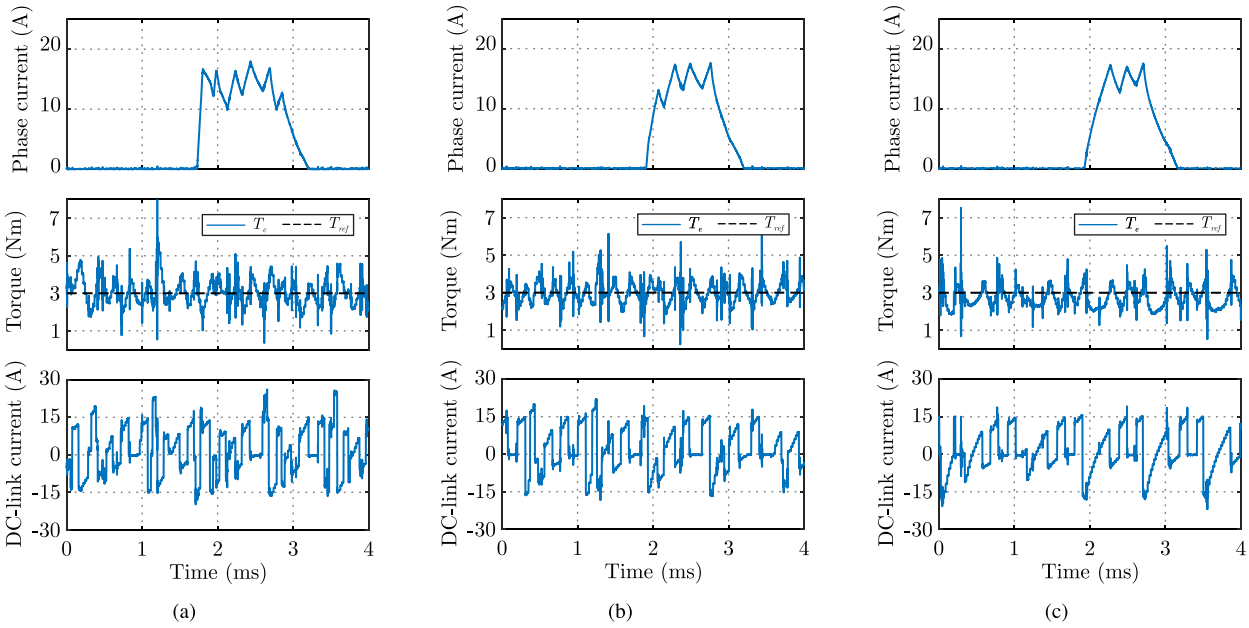

FIGURE 16. Experimental results for SC at a speed of 3000 r/min under a 3 Nm load. (a) Case 1. (b) Case 2. (c) Case 3.

TABLE 5. Performance Comparison for the Experimental Results at a Speed of 1000 r/min Under a 3 Nm Load

Excitation	Case	T_{RMSE} (Nm)	$i_{\text{dc-link}}$ (A)	T_{ripple} (%)	η (%)	$T_{\text{avg}}/i_{\text{rms}}$ (Nm/A)
HC	1	0.7386	14.3055	147.76	50.18	0.3835
	2	0.7400	14.2417	158.50	49.51	0.3768
	3	0.7859	14.1596	161.89	49.62	0.3837
SC	1	0.6212	6.4607	128.38	56.47	0.4039
	2	1.0290	5.5479	170.23	56.97	0.4004
	3	1.0862	5.0718	166.39	55.93	0.4086

TABLE 6. Performance Comparison for the Experimental Results at a Speed of 3000 r/min Under a 3 Nm Load

Excitation	Case	T_{RMSE} (Nm)	$i_{\text{dc-link}}$ (A)	T_{ripple} (%)	η (%)	$T_{\text{avg}}/i_{\text{rms}}$ (Nm/A)
HC	1	0.7562	13.3802	176.27	64.83	0.3999
	2	0.7808	12.8836	219.56	62.57	0.3736
	3	1.1976	11.8778	308.14	57.01	0.2981
SC	1	0.6090	10.1593	201.38	68.21	0.3655
	2	0.5685	9.1485	215.41	68.52	0.3905
	3	0.6045	8.8370	179.73	66.18	0.3709

As seen in Table 5, the expected tradeoff is observed between the three cases at 1000 r/min. For HC, it can be seen that the difference is rather small between each case; however, note that this is expected as the pareto front shown in Fig. 9 also presents a small amplitude variation for both metrics. Regarding the results for SC, a similar tradeoff is observed. Note, however, that the dc-link current is significantly suppressed at the cost of increased torque tracking error. From Table 6, it can be seen that at 3000 r/min the tradeoff is more evident for HC, as expected from the pareto front in Fig. 10. Once more, dc-link current reduction is achieved at the cost of higher T_{RMSE}. Furthermore, it is observed that the absolute values for T_{RMSE} from the experimental results are higher than the ones presented in the pareto fronts. This is justified by the limitations in sampling frequency and hysteresis band of the experiment, which are respectively smaller and greater than the simulation results, in turn leading to a worse tracking performance. A similar trend to the T_{RMSE} metric is observed for the torque ripple measurements. It should be pointed out, however, that the torque ripple metric is often avoided. Given that the metric uses maximum and minimum values, it can be significantly affected by noise or varying peak values in the

measurements, not truly reflecting the characteristics of the output torque, as seen in both speeds for case 2 with SC, for example.

From the efficiency metric, it can be seen that all three cases present a negligible difference between measurements at 1000 r/min. Similarly, at 1000 r/min minimal difference can be seen between the three cases with regards the torque per ampere ratio. Nonetheless, it is observed that SC presents a superior torque per ampere ratio when compared to HC. Similar efficiency levels are also observed between the different cases at 3000 r/min with SC. Note that each case presents different characteristics regarding copper, iron and switching losses, for example, making it reasonable for similar efficiency values to be reached even under different operating conditions. For the results at 3000 r/min with HC, however, note that efficiency is significantly lower for case 3. This is justified by the lower average torque value, also made evident by the much lower torque per ampere ratio. Finally, when comparing HC and SC, it is observed that the latter presents higher efficiency at both speeds. This is expected due to the lower switching frequency, reduced dc-link current and use of the freewheeling state, among other factors.

VI. CONCLUSION

This article investigates the optimization of analytical TSFs aiming to reduce the dc-link current of SRMs. First, a description of the four analytical TSFs is presented, as well as the impact of the excitation parameters in the current profiles. Then, a multiobjective optimization problem taking into account torque rms error and dc-link rms current metrics is solved by means of the NSGA-II algorithm. Next, an approach for selecting a solution with the desired tradeoff from within the pareto front is described. The effectiveness of the proposal is demonstrated by a case study, and further verified by the experimental results, which show the tradeoff between the objectives under three different cases in both hard and SC operation. The combination of parameters selected by the optimization procedure is capable of delivering a performance with adequate balance between both metrics. Furthermore, it can be seen that dc-link current can be effectively reduced with the use of optimized analytical TSFs. Finally, the benefits of dc-link current reduction when using SC over HC are also highlighted. This can consequently enable other drive improvements, such as the increase in capacitor lifetime or capacitor size reduction, two key issues of SRM drives due to the large exchange of energy between the dc-link and the machine. One limitation of the proposal is the fact that it is restricted to the analysis of analytical TSFs. In this context, future work should be carried out in evaluating the dc-link current reduction capabilities of more sophisticated TSFs, such as the ones generated by offline optimization procedures.

REFERENCES

[1] B. Bilgin et al., "Making the case for switched reluctance motors for propulsion applications," *IEEE Trans. Veh. Technol.*, vol. 69, no. 7, pp. 7172–7186, Jul. 2020.

[2] X. Sun, K. Diao, G. Lei, Y. Guo, and J. Zhu, "Direct torque control based on a fast modeling method for a segmented-rotor switched reluctance motor in HEV application," *IEEE Trans. Emerg. Sel. Topics Power Electron.*, vol. 9, no. 1, pp. 232–241, Feb. 2021.

[3] F. P. Scalcon, G. Fang, C. J. V. Filho, H. A. Gründling, R. P. Vieira, and B. Nahid-Mobarakeh, "A review on switched reluctance generators in wind power applications: Fundamentals, control and future trends," *IEEE Access*, vol. 10, pp. 69412–69427, 2022.

[4] L. Ge, Z. Fan, N. Du, J. Huang, D. Xiao, and S. Song, "Model predictive torque and force control for switched reluctance machines based on online optimal sharing function," *IEEE Trans. Power Electron.*, vol. 38, no. 10, pp. 12359–12364, Oct. 2023.

[5] G. Fang, F. P. Scalcon, C. J. V. Filho, D. Xiao, B. Nahid-Mobarakeh, and A. Emadi, "A unified wide-speed range sensorless control method for switched reluctance machines based on unsaturated reluctance," *IEEE Trans. Ind. Electron.*, vol. 70, no. 10, pp. 9903–9913, Oct. 2023.

[6] G. Fang, F. P. Scalcon, D. Xiao, R. P. Vieira, H. A. Gründling, and A. Emadi, "Advanced control of switched reluctance motors (SRMs): A review on current regulation, torque control and vibration suppression," *IEEE Open J. Ind. Electron. Soc.*, vol. 2, pp. 280–301, 2021.

[7] X. Sun et al., "Optimal design of terminal sliding mode controller for direct torque control of SRMs," *IEEE Trans. Transport. Electrific.*, vol. 8, no. 1, pp. 1445–1453, Mar. 2022.

[8] M. Abdalmagid, E. Sayed, M. H. Bakr, and A. Emadi, "Geometry and topology optimization of switched reluctance machines: A review," *IEEE Access*, vol. 10, pp. 5141–5170, 2022.

[9] S. Song, J. Liu, Y. Zhao, L. Ge, R. Ma, and W. Liu, "High-dynamic four-quadrant speed adjustment of switched reluctance machine with torque predictive control," *IEEE Trans. Ind. Electron.*, vol. 69, no. 8, pp. 7733–7743, Aug. 2022.

[10] M. V. De Paula, S. S. Williamson, and T. A. d. S. Barros, "Four-quadrant model following sliding mode cruise control for SRM with DITC applied to transportation electrification," *IEEE Trans. Transport. Electrific.*, vol. 8, no. 3, pp. 3090–3099, Sep. 2022.

[11] D. C. Romero, I. Kortabarria, J. Andreu, F. Rodríguez, A. Arcas, and N. Delmonte, "A methodology to determine the effect of a novel modulation in the reliability of an automotive DC-link capacitor," *IEEE Access*, vol. 8, pp. 192713–192726, 2020.

[12] H. Soliman, H. Wang, and F. Blaabjerg, "A review of the condition monitoring of capacitors in power electronic converters," *IEEE Trans. Ind. Appl.*, vol. 52, no. 6, pp. 4976–4989, Nov./Dec. 2016.

[13] H. Wang and F. Blaabjerg, "Reliability of capacitors for DC-link applications in power electronic converters–An overview," *IEEE Trans. Ind. Appl.*, vol. 50, no. 5, pp. 3569–3578, Sep./Oct. 2014.

[14] S. S. Ahmad and G. Narayanan, "Evaluation of DC-link capacitor RMS current in switched reluctance motor drive," *IEEE Trans. Ind. Appl.*, vol. 57, no. 2, pp. 1459–1471, Mar./Apr. 2021.

[15] A. Klein-Hessling, B. Burkhart, and R. W. De Doncker, "Active source current filtering to minimize the DC-link capacitor in switched reluctance drives," *CPSS Trans. Power Electron. Appl.*, vol. 4, no. 1, pp. 62–71, Mar. 2019.

[16] W. Cai and F. Yi, "An integrated multiport power converter with small capacitance requirement for switched reluctance motor drive," *IEEE Trans. Power Electron.*, vol. 31, no. 4, pp. 3016–3026, Apr. 2016.

[17] F. Yi and W. Cai, "A quasi-Z-source integrated multiport power converter as switched reluctance motor drives for capacitance reduction and wide-speed-range operation," *IEEE Trans. Power Electron.*, vol. 31, no. 11, pp. 7661–7676, Nov. 2016.

[18] D. Cabezuelo, I. Kortabarria, J. Andreu, U. Ugalde, B. Blanqué, and P. Andrada, "Synchronized switching modulation to reduce the DC-link current in SRM drives," *IEEE Access*, vol. 8, pp. 57849–57858, 2020.

[19] C. R. Neuhaus, N. H. Fuengwarodsakul, and R. W. De Doncker, "Control scheme for switched reluctance drives with minimized DC-link capacitance," *IEEE Trans. Power Electron.*, vol. 23, no. 5, pp. 2557–2564, Sep. 2008.

[20] M. E. Haque et al., "DC-link current ripple reduction in switched reluctance machine drives," *IEEE Trans. Ind. Appl.*, vol. 57, no. 2, pp. 1429–1439, Mar./Apr. 2021.

[21] X. D. Xue, K. W. E. Cheng, and S. L. Ho, "Optimization and evaluation of torque-sharing functions for torque ripple minimization in switched reluctance motor drives," *IEEE Trans. Power Electron.*, vol. 24, no. 9, pp. 2076–2090, Sep. 2009.

[22] V. P. Vujičić, "Minimization of torque ripple and copper losses in switched reluctance drive," *IEEE Trans. Power Electron.*, vol. 27, no. 1, pp. 388–399, Jan. 2012.
[23] J. Ye, B. Bilgin, and A. Emadi, "An offline torque sharing function for torque ripple reduction in switched reluctance motor drives," *IEEE Trans. Energy Convers.*, vol. 30, no. 2, pp. 726–735, Jun. 2015.
[24] G. Fang, J. Ye, D. Xiao, Z. Xia, X. Wang, and A. Emadi, "Time-efficient torque shaping for switched reluctance machines from linear space," *IEEE Trans. Power Electron.*, vol. 36, no. 8, pp. 9361–9371, Aug. 2021.
[25] Z. Xia, B. Bilgin, S. Nalakath, and A. Emadi, "A new torque sharing function method for switched reluctance machines with lower current tracking error," *IEEE Trans. Ind. Electron.*, vol. 68, no. 11, pp. 10612–10622, Nov. 2021.
[26] J. Cai and Z. Liu, "An unsaturated inductance reconstruction based universal sensorless starting control scheme for SRM drives," *IEEE Trans. Ind. Electron.*, vol. 67, no. 11, pp. 9083–9092, Nov. 2020.
[27] F. Peng, J. Ye, and A. Emadi, "An asymmetric three-level neutral point diode clamped converter for switched reluctance motor drives," *IEEE Trans. Power Electron.*, vol. 32, no. 11, pp. 8618–8631, Nov. 2017.
[28] K. Deb, A. Pratap, S. Agarwal, and T. Meyarivan, "A fast and elitist multiobjective genetic algorithm: NSGA-II," *IEEE Trans. Evol. Comput.*, vol. 6, no. 2, pp. 182–197, Apr. 2002.
[29] R. Gobbi, N. C. Sahoo, and R. Vejian, "Experimental investigations on computer-based methods for determination of static electromagnetic characteristics of switched reluctance motors," *IEEE Trans. Instrum. Meas.*, vol. 57, no. 10, pp. 2196–2211, Oct. 2008.
[30] F. P. Scalcon, G. Fang, R. P. Vieira, H. A. Gründling, and A. Emadi, "Discrete-time super-twisting sliding mode current controller with fixed switching frequency for switched reluctance motors," *IEEE Trans. Power Electron.*, vol. 37, no. 3, pp. 3321–3333, Mar. 2022.
[31] B. Bilgin, J. Jiang, and A. Emadi, *Switched Reluctance Motor Drives: Fundamentals to Applications*. Boca Raton, FL, USA: CRC Press, 2019.

FILIPE PINARELLO SCALCON (Member, IEEE) received the B.Sc., M.Sc., and Ph.D. degrees in electrical engineering from the Federal University of Santa Maria (UFSM), Santa Maria, Brazil, in 2017, 2019, and 2021, respectively.

He is currently a Postdoctoral Associate with the Department of Electrical and Software Engineering, University of Calgary, Calgary, AB, Canada. He conducted research as a Member of the Power Electronics and Control Research Group, UFSM. From 2022 to 2024, he was a Postdoctoral Fellow with McMaster Automotive Resource Centre, McMaster University, Hamilton, ON, Canada. His research interests include electrical machine drives, renewable energy conversion, microgrids, reluctance machines, and digital control.

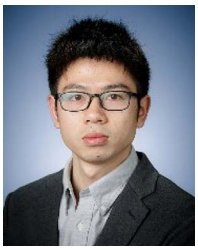

GAOLIANG FANG (Member, IEEE) received the B.S. and M.S. degrees from Northwestern Polytechnical University, Xi'an, China, in 2015 and 2018, respectively, and the Ph.D. degree from McMaster University, Hamilton, ON, Canada, in 2021, all in electrical engineering.

He is currently an Assistant Professor with the Faculty of Sustainable Engineering, University of Prince Edward Island (UPEI), Charlottetown, PE, Canada. Before he joined the UPEI, he was a Postdoctoral Fellow with the McMaster Automotive Resource Centre, McMaster University. During his postdoctoral period, he also interned at Enedym Inc., Hamilton, ON, Canada, under the support of Mitacs Accelerate Fellowship. His research focuses on advanced drive system toward transportation electrification, especially on the advanced control of switched reluctance machines and permanent magnet synchronous machines.

CESAR JOSÉ VOLPATO FILHO (Member, IEEE) received the B.S., M.S., and Ph.D. degrees in electrical engineering from the Federal University of Santa Maria, Santa Maria, Brazil, in 2017, 2018, and 2021, respectively.

He is currently a Control Engineer with Siemens Gamesa, Brande, Denmark. From 2014 to 2021, he was with the Power Electronics and Control Research Group, where he worked on research and development of high performance sensorless control of ac motors. From 2022 to 2023, he was a Postdoctoral Fellow with McMaster Automotive Resource Centre, McMaster University, Hamilton, ON, Canada, where he performed research on control of switched reluctance motors. His research interests include high-performance electric machine drives and applied nonlinear control.

SUMEDH DHALE (Member, IEEE) received the B.E. degree in electrical engineering from the University of Pune, Pune, India, in 2012, the M.Tech. degree in power electronics and drives from VIT University, Vellore, India, in 2015, and the Ph.D. degree in electrical and computer engineering from McMaster University, Hamilton, ON, Canada, in 2021.

He is currently a Principal Controls Engineer with Enedym Inc., Hamilton, ON, Canada, focusing on high-performance control for switched reluctance machine drives and power converters. From 2021 to 2023, he was a Postdoctoral Research Associate with McMaster Automotive Resource Centre, Hamilton, ON, Canada, leading a research collaboration project with Enedym Inc. His research interests include the development of high-performance control, observation, and optimization algorithms for dynamical systems.

BABAK NAHID-MOBARAKEH (Fellow, IEEE) received the Ph.D. degree in electrical engineering with highest distinction from the Institut National Polytechnique de Lorraine, Nancy, France, in 2001, and the HDR (habilitation) degree from the University of Lorraine, Nancy, France, in 2012.

From 2001 to 2006, he was with the Centre de Robotique, Electrotechnique et Automatique, University of Picardie, Amiens, France. In 2006, he joined the Ecole Nationale Superieure d'Electricite et de Mecanique, University of Lorraine, where he was a Professor until 2019. Since 2020, he has been a Professor with McMaster University, Hamilton, ON, Canada. He has authored or coauthored more than 300 international peer-reviewed journal and conference papers as well as several book chapters. His research interests include nonlinear and robust control design for power converters and motor drives, fault detection and fault-tolerant control of electric systems, and design, control, and stabilization of microgrids.

Dr. Nahid-Mobarakeh was the recipient of several IEEE awards and holds 28 published patents. He has chaired several conferences in the area of the control and electrification of transportation systems. Furthermore, he served as an Executive Officer, then the Chair of the Industrial Automation and Control Committee (IACC) of the IEEE Industry Applications Society (IAS) between 2012 and 2019. He was also the IACC Committee Administrator and Technical Committee Paper Review Chair of the IEEE IAS. He is currently the Vice Chair of the IEEE Power Electronics Society Technical Committee on Electrified Transportation Systems (PELS TC4). He is also a Member of the Power Electronics and Motion Control (PEMC) Council.